INL/JOU-20-59180-Revision-0

The influence of lattice defects, recombination, and clustering on thermal transport in single crystal thorium dioxide

November 2020

Changing the World's Energy Future

Cody Andrew Dennett, Zilong Hua, Amey Rajendra Khanolkar, Tiankai Yao, Timothy A. Prusnick, Phyllis K. Morgan, Narayan Poudel, Aaron French, Krzysztof Gofryk, Lingfeng He, Lin Shao, Marat Khafizov, J. Matthew Mann, David H Hurley, David B. Turner

Idaho National Laboratory

INL/JOU-20-59180-Revision-0

The influence of lattice defects, recombination, and clustering on thermal transport in single crystal thorium dioxide

Cody Andrew Dennett, Zilong Hua, Amey Rajendra Khanolkar, Tiankai Yao, Timothy A. Prusnick, Phyllis K. Morgan, Narayan Poudel, Aaron French, Krzysztof Gofryk, Lingfeng He, Lin Shao, Marat Khafizov, J. Matthew Mann, David H Hurley, David B. Turner

November 2020

Idaho National Laboratory
Idaho Falls, Idaho 83415

http://www.inl.gov

Prepared for the
U.S. Department of Energy
Under DOE Idaho Operations Office
Contract DE-AC07-05ID14517

The influence of lattice defects, recombination, and clustering on thermal transport in single crystal thorium dioxide

Cody A. Dennett,[1,*] Zilong Hua,[1] Amey Khanolkar,[1] Tiankai Yao,[2] Phyllis K. Morgan,[3] Timothy A. Prusnick,[3,4] Narayan Poudel,[5] Aaron French,[6] Krzysztof Gofryk,[5] Lingfeng He,[2] Lin Shao,[6] Marat Khafizov,[7] David B. Turner,[3,8] J. Matthew Mann,[3] and David H. Hurley[1]

[1]*Materials Science and Engineering Department, Idaho National Laboratory, Idaho Falls, ID 83415, USA*
[2]*Characterization and Advanced Post-Irradiation Examination, Idaho National Laboratory, Idaho Falls, ID 83415, USA*
[3]*Air Force Research Laboratory, Sensors Directorate, Wright-Patterson AFB, OH 45433, USA*
[4]*KBR, Dayton, OH 45431, USA*
[5]*Nuclear Materials Department, Idaho National Laboratory, Idaho Falls, ID 83415, USA*
[6]*Nuclear Engineering Department, Texas A&M University, College Station, TX 77843, USA*
[7]*Department of Mechanical and Aerospace Engineering, The Ohio State University, Columbus, OH 43210, USA*
[8]*Azimuth Corporation, Beavercreek, OH 45431, USA*
(Dated: September 21, 2020)

Thermal transport is a key performance metric for thorium dioxide in many applications where defect-generating radiation fields are present. An understanding of the effect of nanoscale lattice defects on thermal transport in this material is currently unavailable due to a lack of single crystal material from which unit processes may be investigated. In this work, a series of high-quality thorium dioxide single crystals are exposed to 2 MeV proton irradiation at room temperature and 600°C to create microscale regions with varying densities and types of point and extended defects. Defected regions are investigated using spatial domain thermoreflectance to quantify the change in thermal conductivity as a function of ion fluence as well as transmission electron microscopy and Raman spectroscopy to interrogate the structure of the generated defects. Together, this combination of methods provides important initial insight into defect formation, recombination, and clustering in thorium dioxide and the effect of those defects on thermal transport. These methods also provide a promising pathway for the quantification of the smallest-scale defects that cannot be captured using traditional microscopy techniques and play an outsized role in degrading thermal performance.

I. INTRODUCTION

Actinide and lanthanide fluorite oxides, ThO_2, UO_2, and CeO_2, form an important family of high temperature ceramics for a variety of energy applications. UO_2 forms the basis for the large majority of commercial nuclear fuels worldwide [1]. CeO_2 is utilized in electrochemical applications, as a catalysis material due to its ability to store and transport oxygen, and as a solid oxide fuel cell material [2–4]. Given these technological implications, the thermophysical properties and performance characteristics of UO_2 and CeO_2 have been the subject of detailed study for decades [5–8]. In contrast, ThO_2 has been less widely investigated to date despite potential applications as a fertile fuel in advanced, proliferation-resistant nuclear reactors [9–11] and as a high reflectivity material for extreme ultraviolet optics [12]. Exhibiting similar behavior in many respects, ThO_2 has several key distinctions from other heavy metal fluorite oxides that make it attractive for the above mentioned applications including a fixed tetravalent cation oxidation state, extremely high melting temperature, and large electronic bandgap [13,14]. For many of these applications, thermal transport is a key property that determines the suitability of a particular oxide for a particular use, controlling, for example, the peak center line temperature in nuclear fuels and heat dissipation ability in large bandgap electronics.

Potential operating environments for these materials include high radiation fields and extreme temperatures that promote or directly generate lattice defects in otherwise perfect fluorite structures. These nanoscale to microscale features have been revealed to drastically reduce thermal conductivity [15–18]. However, it has been shown in actinide and lanthanide oxides that the largest effects on thermal transport are often caused by the smallest-scale lattice defects at the earliest stages of damage accumulation [18]. Characterizing both the size and concentration of these types of defects is challenging as statistically-significant populations of defects cannot be imaged directly using ultrahigh resolution microscopy. Therefore, indirect methods must be used to characterize the presence of these sub-resolution defects. Positron annihilation spectroscopy (PAS) has been used to characterize defects on the smallest scales, however PAS is only sensitive to vacancy-type defects and cluster type discrimination is difficult [19]. Synchrotron-based methods including X-ray diffraction (XRD) [20] and absorption methods [21] have also been used to collect detailed local

* cody.dennett@inl.gov

defect structures in fluorite oxides. For both UO_2 and CeO_2, combinations of more easily-implemented bench-top methods including XRD [22], Raman scattering [23], and other optical techniques [24] have been used to characterize defect populations in these oxides. One notable recent example is the work of Khafizov and coworkers who used a combination of microscale thermal transport measurements and XRD to infer features of nanoscale defect evolution in ion-irradiated UO_2 [25]. While important inroads have been made in understanding the role of small-scale defects on thermal transport in UO_2, a similar level of experimentally-validated understanding for ThO_2 is lacking [16,26–29]. This deficit largely stems from the inability to grow high-quality single crystals of ThO_2 with confirmed crystal orientation, purities, and stoichiometries [30]. Such high-quality material is required for a detailed investigation of the effects of nanoscale defects as contributions from impurity and grain boundary scattering present in more commonly used sintered ThO_2 samples may occlude conductivity reduction from defect formation and agglomeration.

In this work, a series of high-quality single crystal ThO_2 specimens are subject to ion beam irradiation as a tool to create a microscale region with varying levels of defect concentrations. These exposures are conducted at both room temperature and 600°C to explore the influence of defect recombination and clustering on thermal transport. Given the extremely high melting temperature of ThO_2 ($T_m = 3390$°C), it is unknown *a priori* whether the high temperature exposures conducted here will result in recombination and clustering into nanoscale defect clusters or dislocation loops [15]. While some authors have identified defect annealing in ThO_2 at temperatures lower than 600°C [31,32], others have calculated high migration energies for oxygen and thorium defects (1.3–2.2 eV and ∼4.5 eV, respectively), suggesting the mobility of irradiation-induced defects should be low [33,34].

Following ion beam exposure, the thermal diffusivity of the approximately 20 µm thick defected surface layer is measured using an all-optical modulated thermoreflectance methodology at room temperature [35]. In addition, transmission electron micrographs are captured of the defected layer of samples exposed at 600°C to determine if radiation-induced dislocation loop formation has occurred [36–38]. Finally, top-down Raman spectra are collected and interpreted with respect to features observed in other heavy metal fluorite oxides to shed light on the character of the generated defect populations. Together, these methods provide important initial insight into the types of defects formed under irradiation, defect clustering, and how these defects impact thermal transport in high-quality ThO_2.

II. MATERIALS AND METHODS

Single crystals of thorium dioxide were grown using the hydrothermal synthesis method in an inert silver ampoule [30]. A feedstock of 20.25 g of ThO_2 powder (99.99% pure, International Bio-analytical Laboratories) was placed in the bottom of the ampoule along with 62 mL of six molar cesium fluoride solution (Alfa Aesar, 99.99%). A silver baffle was placed in the middle of the silver ampoule to separate the feedstock zone from the crystallization zone in the upper section of the ampoule. The ampoule was welded shut and placed into an Inconel autoclave with counter pressure water added between the ampoule and the interior walls of the autoclave to prevent rupturing. Band heaters were placed on the exterior walls of the autoclave with the height corresponding with the feedstock and crystallization zones in the ampoule, which were held at 750°C and 690°C, respectively. This generated a pressure within the autoclave of 18 kpsi. These conditions were maintained for 10 days before the reaction was allowed to return to room temperature over a 24 hour period. The ThO_2 crystals were retrieved from the ampoule and washed thoroughly with deionized water and acetone to remove excess thorium oxide powder and residual cesium fluoride mineralizer. Impurity levels in an as-grown crystal were investigated using X-ray fluorescence spectrometry (XRF) and time-of-flight secondary ions mass spectrometry (TOF-SIMS). The impurity concentration is estimated to be ∼0.37 at% through the bulk of the crystals, mostly from native impurities in the ThO_2 feedstock and the cesium fluoride mineralizer. Details of the impurity analysis can be found in the Supplementary Information. Single crystals with {001} orientation were selected based on the morphology of the crystals and the angle between crystal facets and mounted on copper blocks using silver paste prior to ion beam exposure.

Five mounted samples were exposed to 2 MeV protons (H^+ ions) at both room temperature (3 samples) and 600°C (2 samples) using the 3 MV tandem pelatron accelerator at Texas A&M University. Samples were exposed to a rastered ion beam with a 20% overscan of each crystal face to ensure a uniform dose across the sample surface with a flux of 1.8×10^{13} ions/cm^{2}s. The sample temperature was monitored during irradiation by a thermocouple press-fit to the copper mounting block for control at high temperatures and to ensure no significant ion beam heating occurred at room temperature. The depth distribution of damage induced by the proton beam was calculated using the Stopping Range of Ions in Matter (SRIM) code in the full cascade mode using the theoretical density of ThO_2 and displacement energies of $E_d = 48.5$ eV and 17.5 eV for thorium and oxygen respectively [39–41]. Prior to exposure, target ion fluence levels were selected in the range of $1.7\times10^{17} - 1.7\times10^{18}$ ions/cm^2 for room temperature exposures and $5.1 - 8.6\times10^{18}$ ions/cm^2 for 600°C exposures based on prior measurements of thermal conduc-

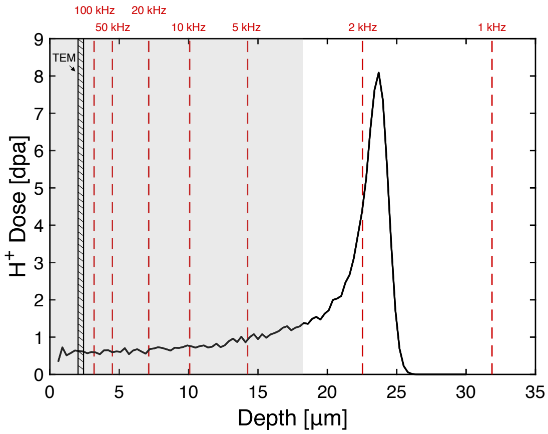

FIG. 1. Depth-dependent damage profile of 2 MeV H^+ ions into ThO_2 as calculated using full cascade SRIM simulations scaled to the highest-fluence exposure (8.6×10^{18} ions/cm^2). The "plateau" region identified for damage estimation in dpa is shaded. Thermal penetration depths, L_{th}, are indicated as dashed vertical lines for two orders of magnitude of SDTR measurement frequencies calculated using highest measured diffusivity of any irradiated sample ($D = 3.19$ mm^2/s). The hatched region indicates the approximate depth from which TEM lamella were lifted out.

tivity reduction in isostructural systems at similar dose levels [18,38]. Given the peak displacement damage at 24 µm, as seen in Fig. 1, a "plateau" damage region was identified consisting of an 18 µm surface layer of the exposed samples. For this plateau region, Table I lists the average dose in displacements per atom (dpa) for each exposure. Using this metric, the doses investigated in this study range from 0.016–0.79 dpa.

Following ion irradiation, the room-temperature thermal diffusivity of the ion-modified surface layer of the ThO_2 specimens was measured using the spatial domain thermoreflectance (SDTR) technique [35]. In this method, an intensity modulated 660 nm continuous wave (CW) laser is focused to an approximately 2 µm spot on the surface of the sample under investigation using a 50× objective lens. A 532 nm detection laser is used as a temperature probe by detecting small changes in optical reflectivity due to the periodic temperature field driven by the heating laser. The optical power at the sample surface for these measurements is ∼4 mW and ∼0.5 mW for the heating and detection laser, respectively. Lock-in detection is used to determine the phase lag between heating and detection lasers as a function of spatial separation. In order to ensure a sufficient thermoreflectance response, samples are coated with a thin layer of gold as a transducer. The thickness of this layer varied between 7 and 34 nm for the samples measured here. The thermal properties of the deposited gold films were determined from co-deposited films of the same thickness on pristine NBK7 substrates. The details of this procedure and the measured film properties are outlined in the Supplementary Information.

For these experiments, the measured far-field thermal wave profiles are used to extract the thermal diffusivity of the irradiated layer [35,42]. The details of the parameter extraction procedure are described in the Supplementary Information. Optimized values of thermal diffusivity are then converted to thermal conductivity explicitly using a theoretical density of 10.05 g/cm^3 and room temperature heat capacity of $c_p = 230.1$ J/kg·K measured from pristine ThO_2 using a Quantum Design Dynacool-9 system and the two-tau relaxation technique [43]. Temperature-dependent values for c_p in the range 2–302 K are also provided in the Supplementary Information. To ensure that thermal properties of only the ion-modified surface layer are measured, the depth of the identified plateau region must be compared with the penetration depth of the applied thermal wave. This depth is given as $L_{th} = \sqrt{D/\pi f}$, where D is the thermal diffusivity and f is the frequency of the modulation [44,45]. To identify an appropriate frequency range for measurement, the thermal penetration depth for commonly-used SDTR modulation frequencies between 1 and 100 kHz are calculated for the irradiated sample with the highest measured diffusivity and plotted on top of the SRIM-calculated damage profile in Fig. 1. This analysis makes clear that modulation frequencies of 5 kHz and above are well-suited for diffusivity measurements of irradiated materials for these conditions [46,47]. Thermal diffusivity values are therefore determined from 4-12 SDTR scans of 4-5 frequencies each in the range 5-100 kHz.

In addition to thermal property characterization, direct imaging of any dislocation loop formation in samples exposed at 600°C was conducted using transmission electron microscopy (TEM). Initial high-resolution TEM (HRTEM) of the highest dose sample irradiated at room temperature, RT03, revealed no defect clusters. As such, further TEM investigation of samples exposed at room temperature was not pursued. Cross sectional samples perpendicular to proton-irradiated surface taken from 2 µm below that surface, see Fig. 1, were prepared using a FEI 3D Quanta focused ion beam (FIB) system. This region is far enough from the surface to avoid any denuded zone that may be present and lies within the identified plateau region. Samples were thinned to a final thickness of roughly 40 nm using 30 keV Ga ions with a final cleaning conducted using 2 keV Ga ions. An FEI Titan Themis 200 TEM was used for bright-field TEM and high resolution TEM (HRTEM) imaging to observe dislocation loops. Image analysis and measurements of dislocation loop size and density were conducted manually using ImageJ [48]. Electron energy loss spectroscopy (EELS) was used to determine the thickness of the FIB lamina using reported values of the inelastic mean free path for electrons in ThO_2 [49].

Finally, four of the five irradiated ThO_2 specimens were characterized using Raman spectroscopy pre- and post ion beam exposure [50]. One irradiated sample was gold coated for thermal property characterization immediately following irradiation, precluding post-exposure

Sample ID	Ion Fluence [ions/cm^2]	Plateau Dose [dpa]	Irradiation Temperature	Au Film Thickness [nm]
pristine	–	–	–	7
RT01	1.727×10^{17}	0.016	Room Temp.	17
RT02	8.635×10^{17}	0.079	Room Temp.	17
RT03	1.727×10^{18}	0.16	Room Temp.	34
HT01	5.181×10^{18}	0.47	600°C	17
HT02	8.635×10^{18}	0.79	600°C	17

TABLE I. Sample list including ion fluence, calculated dose in dpa, exposure temperature, and the thickness of the gold film deposited post-exposure to aid in SDTR measurements. Samples have been assigned an ID for reference within the text.

Raman measurements. Raman spectra were collected in a top-down geometry with excitation lasers focused at the crystal surface using Renishaw Invia Reflex system with a 50× long working distance objective and a 65 µm slit width. Spectra were collected using both a 632.8 nm excitation laser at ∼4 mW coupled to a 1200 l/mm grating and a 532 nm excitation laser at ∼2.5 mW coupled to a 1800 l/mm grating for each sample. Gratings were centered at 1000 cm^{-1} and each spectrum is the accumulation of three 5 sec exposures. The Raman system was calibrated to single crystal silicon prior to each measurement. To ease in interpretation of defect-induced Raman features, raw spectra were baseline corrected using the adaptive iteratively reweighted Penalized Least Squares (airPLS) algorithm [51]. Raw Raman spectra as well as a graphical example of the baseline subtraction process are provided in the Supplementary Information.

III. EXPERIMENTAL RESULTS

A. Thermal transport analysis

The results of SDTR thermal transport analysis of proton irradiated ThO_2 are summarized in Fig. 2. Example SDTR scans at 5 frequencies on the most highly irradiated sample under consideration (HT02) are shown in Fig. 2(a). The region between the vertical lines denotes the near-field thermal wave region and is set as 8 µm (four times the convolved laser spot size) for all samples except RT03, which was measured prior to an optical system optimization and appears to have a larger effective spot size. For that sample only, the near-field region is extended to 10 µm. The overlaid dashed lines represent the 10 segments (2× the number of frequencies measured) which are co-optimized to a single value of ThO_2 diffusivity. For all SDTR measurements, this global optimization results in slopes which quite accurately capture the far-field phase lag for multiple frequencies simultaneously. The average Jacobian estimate of the 2σ confidence interval on the optimized thermal diffusivity values across all measurements is 6.5%. The measured thermal diffusivity values for all samples averaged across multiple spatial locations are given in Table II.

Fig. 2(b) compares phase profiles for three samples (pristine, RT01, HT02) at 20 kHz. As the phase lag increases as thermal diffusivity decreases, this comparison shows clearly that HT02 has retained a greater thermal diffusivity than RT01 despite receiving more than fifty times more ion fluence, as listed in Table I. The thermal conductivity as a function of the received radiation dose in dpa is plotted in Fig. 2(c). The room temperature conductivity of the pristine single-crystal thoria is measured as $\kappa_0 = 18.6$ W/m·K, which matches previously-reported values from Mann and coworkers on similarly-grown single crystal specimens [30]. All three samples irradiated at room temperature show a dramatic decrease in thermal conductivity to only 20-25% of the pristine value. In contrast, samples irradiated at 600°C retain approximately 40% of the thermal conductivity of pristine ThO_2. The fractional conductivity, κ/κ_0, for each exposure condition is listed in Table II.

Sample ID	Measured Diffusivity [mm^2/s]	κ/κ_0
Pristine	8.06 ± 0.55	–
RT01	2.06 ± 0.14	0.26 ± 0.03
RT02	1.58 ± 0.09	0.20 ± 0.02
RT03	1.77 ± 0.32	0.22 ± 0.04
HT01	3.19 ± 0.21	0.40 ± 0.04
HT02	3.05 ± 0.31	0.38 ± 0.05

TABLE II. Measured room temperature thermal diffusivity and fractional conductivity for each of the exposure conditions investigated. Uncertainties in measured diffusivity are given as the standard deviation of between 4 and 12 spatially-varying multi-frequency SDTR measurements, and uncertainties in fractional conductivity account for input uncertainties in both pristine and defected diffusivity measurements.

B. Transmission electron microscopy

TEM characterization carried out on ThO_2 samples exposed at 600°C reveals a high density of radiation-induced dislocation loops. Fig. 3(a) and (c) show bright field (BF) images of both HT01 and HT02 samples. The dislocation loop size and density were measured from these BF images. For HT01 the average dislocation loop radius is 3.1 ± 0.9 nm and for HT02 that radius is 2.6 ± 0.6 nm where the uncertainty is given as the standard deviation in measured loop sizes. The disloca-

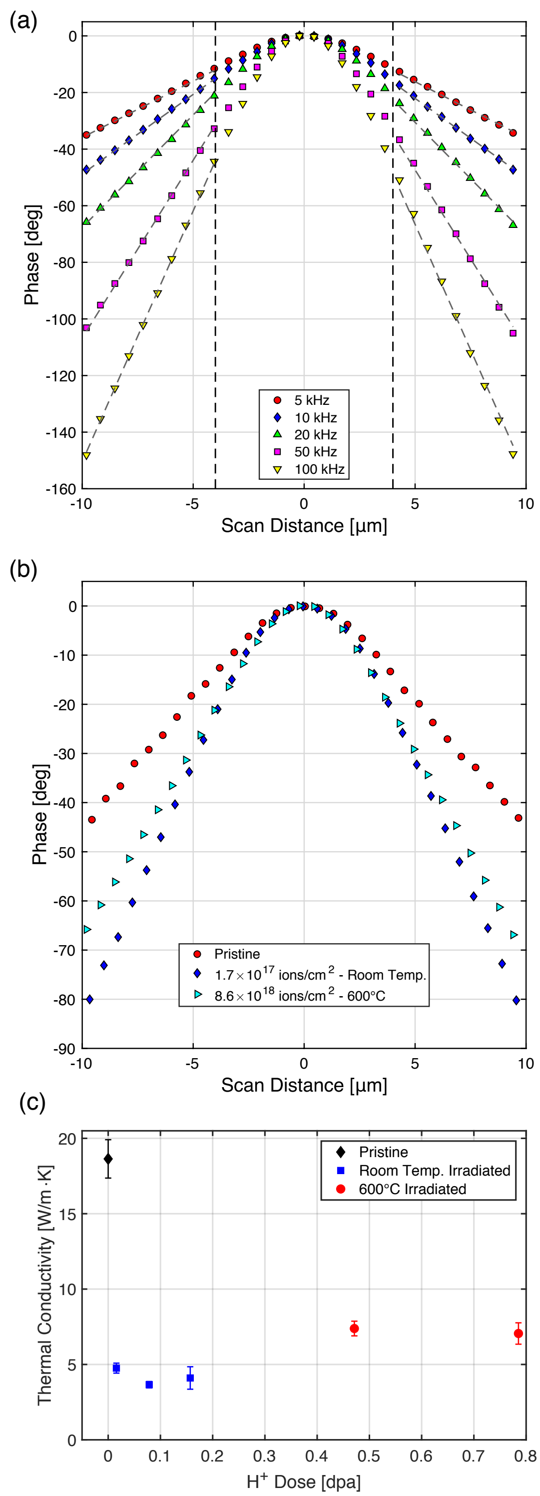

FIG. 2. (a) Example SDTR data including the output of the global far-field optimizer for D_s as measured on HT02. (b) Comparison of 20 kHz phase profiles for pristine, RT01, and HT02 samples showing that samples exposed at 600°C retained a higher thermal diffusivity than those exposed at room temperature. (c) Thermal conductivity as function of plateau region radiation dose in dpa in single crystal ThO_2.

tion loop density is also calculated by using the EELS-measured lamella thicknesses (∼32 and ∼43 nm, respectively, for HT01 and HT02) as $(3.5 \pm 0.7) \times 10^{22}$ 1/m^3 for HT01 and $(5.2 \pm 0.8) \times 10^{22}$ 1/m^3 for HT02 where the standard deviation is calculated using counting statistics and assuming a 10% error in the measured thickness [52]. No voids or vacancy clusters have been observed. High-resolution TEM, Fig. 3(b), of HT01 shows that some loops reside on the {111} family of planes. In two works, Khafizov and Chauhan have observed similar {111} loops in CeO_2 irradiated with protons at 600°C and 700°C and identified them as faulted Frank loops [15,53]. In CeO_2 at 600°C and 0.14 dpa, loops are observed with a larger average size of 3.6 nm and lower density of 0.65×10^{22} 1/m^3 compared to the ∼3 nm radius and 3–5 × 10^{22} 1/m^3 density observed here at 0.47 and 0.79 dpa [53]. A further detailed analysis of the dislocation loops formed in these samples to identify their nature in detail, Burgers vector, habit plane, etc., is beyond the scope of the present work. Without this detailed information, the average loop size calculation performed here may be considered an estimate and the density calculation considered a lower bound on the total loop density possibly present.

C. Raman spectroscopy

Raman spectra collected from the pristine, RT01, RT02, HT01, and HT02 samples are shown in Fig. 4 for both 532 and 633 nm laser excitation. For pristine ThO_2, the fluorite lattice structure contains only one Raman-active mode, the T_{2g}, which is observed in both the 532 nm and 633 nm data at approximately 465 cm^{-1} [54]. All baseline-corrected Raman spectra in Fig. 4 have been normalized to the intensity of this T_{2g} peak. As defects are generated under irradiation exposure, new peaks are generated in broad bands from 135 to 210 cm^{-1} and 500 to 645 cm^{-1} which have been shaded for ease of view. These peaks can broadly be denoted as "defect peaks" as they only occur in the defective fluorite structure. Qualitatively, at both wavelengths the intensity of these defect peaks increases relative to T_{2g} as the ion fluence is increased. The effect of increasing defect density is also observed in the broadening of the T_{2g} peak with respect to the pristine spectra. At the highest fluences, the 532 nm spectra also show evidence of shoulder/doublet formation within the T_{2g} peak itself. Due to the top-down geometry used in this investigation, this shoulder/doublet may be due to the Raman response of the damaged surface region and the undamaged bulk being captured simultaneously.

A detailed analysis of the observed defect peaks is complicated by the lack of previous detailed Raman investigation into defect-bearing ThO_2. However, available literature on defected isostructural systems with similar characteristics, primarily UO_2, but also CeO_2 and PuO_2, allow us to make an initial interpretation of the Raman spectra captured here. Defect peak locations observed in

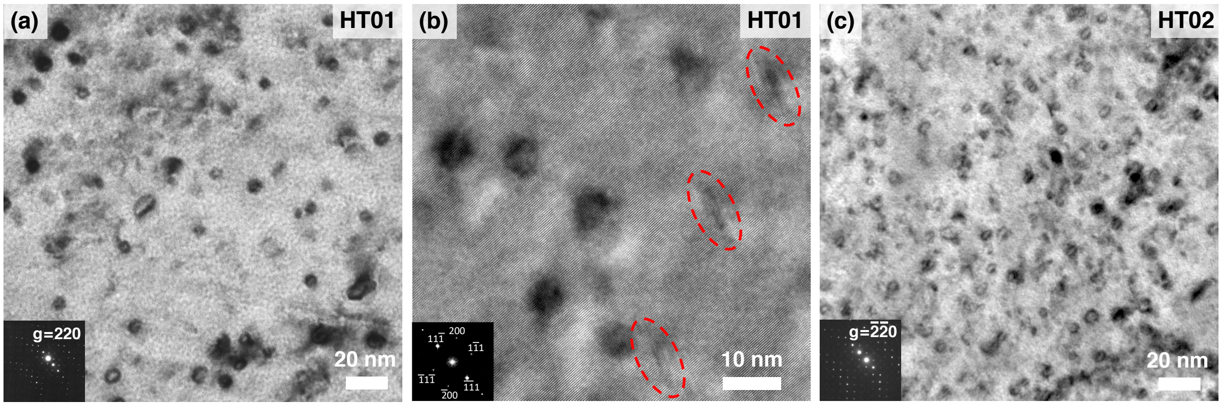

FIG. 3. TEM images HT01 and HT02 showing significant dislocation loop formation. (a) Bright field image of HT01 at $g = 220$ near the [001] zone axis, (b) HRTEM of HT01 near the [011] zone axis (faulted loops on {111} planes circled by red ovals) and (c) bright field image of HT02 at $g = \bar{2}\bar{2}0$ near the [001] zone axis. Insets in (a) and (c) are the selected area electron diffraction (SAED) patterns and inset in (b) is a fast Fourier transform (FFT) of the image.

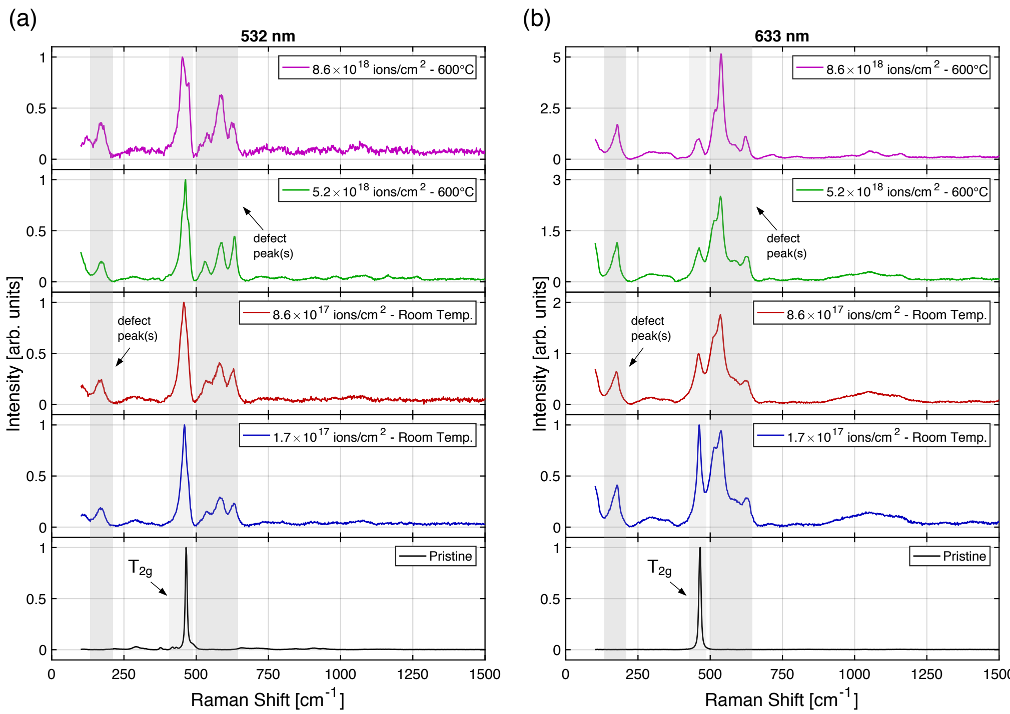

FIG. 4. Raman spectra of pristine and post-irradiated single crystal ThO_2 collected with both (a) 532 nm and (b) 633 nm laser excitation. All data are baseline corrected and normalized to the intensity of the only Raman-active mode of the initial perfect fluorite structure, T_{2g}. This peak and bands of defect peaks are shaded for ease of identification.

Fig. 4 largely correlate with a mixture of hypo- (ThO_{2-x}) and hyperstoichiometric (ThO_{2+x}, Th_4O_9) defect clusters [23,50,55–62]. Unlike uranium, however, thorium has a stable tetravalent oxidation state in oxides and thus would be unlikely to adopt a Th_4O_9 structure. However, both Tracy [63] and Palomeras [64] have postulated local regions of hypo- and hyperstoichiometric defects to exist in a nominally stoichiometric ThO_2. The existence of stable dimers, peroxides, and other charged oxygen interstitial defects in the ThO_2 lattice around regions of hypo- and hyperstoichiometry have also been predicted via DFT calculations [65,66].

Should these local non-stoichiometric regions be present, the Raman peak observed at $\sim$630 cm^{-1} is likely due to interstitial-type defect clusters with cuboctahedral coordination reflecting a Th_4O_9 complex [57,67]. The low wavenumber peak observed at roughly 175 cm^{-1} has similarly been attributed to longer-range M_4O_9 coordination in uranium dioxide [57]. In addition to these defect-cluster-correlated peaks, the peak observed strongly in the 532 nm spectra and more weakly in the 633 nm spectra at approximately 585 cm^{-1} corresponds closely to the T_{1u} symmetry IR-active longitudinal optical (LO) mode determined by optical ellipsometry on similarly-grown pristine ThO_2 single crystals [68]. This mode is not Raman-active in a pristine fluorite lattice, but has been shown to become Raman active in defected UO_2 and CeO_2 due to a breakdown in selection rules [23,55,69,70]. The addition of scattering sites away from the Brillouin zone center caused by vacancies or point defect pairs has been proposed as a likely cause for this selection breakdown [60,71,72].

A significant peak observed in both 532 and 633 nm spectra at 535 cm^{-1} does not correspond to either of the assignments above. Similarly-located peaks have been observed in both ion irradiated UO_2 (denoted U1 at $\sim$530 cm^{-1} [73]), self-damaged PuO_2 (at 540 cm^{-1} [74]), and rare-earth doped UO_2 (at $\sim$530 cm^{-1} [75]). In UO_2 specifically, this peak has been attributed to polyhedra with U^{3+} coordination [73]. However, a consensus for the origin of this feature has not been reached in other isostructural actinide oxides [74]. Accordingly, we will not propose an assignment of this peak to a particular defect type in ThO_2 but simply note that similar features have been observed in other defected fluorite actinide oxides. In addition, a final peak appears in the defected spectra around 515 cm^{-1} as a shoulder on the 535 cm^{-1} peak in all 633 nm data as well as faintly in the HT02 532 nm spectrum. This peak lacks a strong corollary with any vibrational Raman mode observed in defected UO_2 or other isostructural systems. A detailed peak-fitting analysis to determine defect peak intensities as a function of ion fluence is not appropriate for the present data due to complications arising from uncertain signal collection depths, as mentioned above.

IV. DISCUSSION

Our assignment of the 175, 585, and 630 cm^{-1} Raman peaks observed here as directly defect-correlated in keeping with previous studies of UO_2 and CeO_2 conflicts with conclusions by Mohun and coworkers on the Raman spectra of sintered ThO_2 exposed to 21 MeV He^{2+} ions [76]. In that study, peaks at 514, 539, 590, and 622 cm^{-1} under 633 nm excitation were attributed to luminescence induced by the laser. The authors of that study conclude a luminescence effect as the most likely cause due to *in situ* observations of ion beam luminescence during irradiation, color change in the as-irradiated specimens, and a shift in the Raman peak locations from 532 to 633 nm laser excitation. In the present data, although relative peak intensities are observed to shift between 532 and 633 nm excitations consistent with wavelength-dependent Raman responses in similar systems [50,57,74], the peak locations are not observed to vary dramatically between excitation wavelengths. Spectra are captured here with a significantly higher signal-to-noise ratio than Mohun's data given enhanced quality of our single-crystal starting material, particularly at 532 nm. It should be noted, however, that we do observe the same color change from translucent to deep blue in the as-irradiated samples as observed by Mohun and other authors [76,77]. Given the similarity to work in UO_2 and CeO_2, we believe that the majority of the features observed here should be correlated with cuboctahedral clusters and point defects in ThO_2. The 515 cm^{-1} peak observed both here and by Mohun, however, does not have a counterpart in other defected fluorite oxides.

The observed differences in conductivity reduction most likely stem from differences in defect recombination and clustering at the two different exposure temperatures. While the HT samples received higher doses (0.47–0.79 dpa), the retained conductivity is uniformly higher than the RT samples (0.016–0.16 dpa). This suggests clustering of irradiation-induced defects and an overall reduction in phonon scattering for the high temperature samples. The nature of clusters in ThO_2 smaller than the observed dislocation loops has received little attention relative to isostructural systems, particularly UO_2 [78,79]. However, a recent study by Jin et al. provides some insight, suggesting that cuboctahedral clusters may be a prevalent and stable cluster geometry for ThO_2 [67]. That conclusion is supported by the features observed in the Raman analysis undertaken here, specifically peaks at 175 and 630 cm^{-1} related to M_4O_9 complexes.

Considering the Raman spectra, TEM micrographs, and thermal conductivity together allows some insight into the overall formation, agglomeration, and recombination pathway of irradiation induced defects. Qualitatively, the intensity of major irradiation-induced Raman defect bands seem to grow with respect to T_{2g} as the total ion fluence is increased for all samples. In addition, TEM analysis shows that at high temperatures a significant dislocation loop density has been generated under these conditions. High anion defect mobilities in ThO_2 have been observed experimentally previously by Palomares and coworkers. Over multiple studies on swift heavy ion irradiated ThO_2 with a low theoretical density, they have shown significant defect annealing occurs at temperatures above approximately 275°C and attribute this annealing to co-migration of anion vacancies and interstitials as cation mobilities are assumed to be low [31,32,34]. The effect observed here, improving thermal performance by concentrating defects into larger structures and reducing the total number of phonon scattering sites, has been observed previously in both ceramics and metals [26,36,80]. Therefore, we postulate that it is the retained non-loop defect clusters, likely with cuboctahedral coordination, in the 600°C irradiations that are primarily responsible for the continued increase in relative Raman peak intensity with dose.

The average size and density of dislocation loops observed in HT samples also allow us to draw relative conclusions about cation defect mobilities in ThO_2 compared to isostructural systems. {111}-type stoichiometric Frank loops as observed in these samples are comprised of three alternating layers of oxygen-metal-oxygen interstitials in the fluorite structure [81]. This implies that not only are anion defects highly mobile, but also that cation interstitials have sufficient mobility at 600°C to nucleate these loops; the mobility of these cation interstitials should be the rate-limiting step to loop formation and growth given the difference in previously-calculated migration energies [33,34]. Other mechanisms for stoichiometric loop formation in ionic crystals with low cation mobilities have also been proposed, such as the "coercion" mechanism of Hobbs et al. [82], which could play a role in the formation process of these loops. Nevertheless, the high loop density and smaller loop size observed here in ThO_2 at 600°C compared to those observed in CeO_2 and UO_2 at similar conditions is consistent with the assumption that thorium defects should have relatively larger migration energies compared to cerium and uranium defects due to their fixed oxidation state [15,53,83]. However, that loops are observed in these conditions with radii on the order of 3 nm and densities on the order of 10^{22} 1/m^3 implies that cation defect mobilities are possibly higher under these specific ion-irradiation conditions than suggested by modeling [34].

V. CONCLUSIONS AND FUTURE

In this work, the initial study of the effect of irradiation-induced lattice defects on the thermal conductivity of high-quality, single crystal thorium dioxide has been presented. By using spatial domain thermoreflectance, the thermal transport properties of a microscale region exposed to lattice damage via energetic protons was investigated. Post-exposure transmission electron microscopy of the high temperature samples revealed a high density of small dislocation loops and top-down Raman spectroscopy showed characteristic features of defected heavy metal fluorite oxides. This experimental works serves to narrow the future parameter space of interest for low-dose defect effects on transport in ThO_2 as well as define additional investigative pathways to more thoroughly determine the structure and concentration of irradiation induced defects. Moving forward, future studies will include temperature dependent thermal transport measurements to isolate scattering mechanisms, more detailed, depth dependent TEM and (cross-sectional) Raman analysis of defects, and luminescence studies to interrogate the charged defects likely present in ThO_2. The combination of methodologies employed here, used on high quality single crystal ThO_2 specimens, promises a route to accurately treat the complexity of thermal transport in the presence of irradiation-induced defects and to generate insight into the formation and agglomeration pathways of those defects.

SUPPLEMENTARY MATERIAL

See the supplementary information for impurity analysis of the as-grown ThO_2 crystals, a description of the optimization process for determining thermal diffusivity from SDTR data, measured thermal conductivities of thin deposited gold films, temperature-dependent heat capacity of pristine ThO_2, and a description of the Raman baseline subtraction and normalization process.

ACKNOWLEDGMENTS

This work was supported by the Center for Thermal Energy Transport under Irradiation (TETI), an Energy Frontier Research Center funded by the US Department of Energy, Office of Science, Office of Basic Energy Sciences. This work was also supported, in part, by the US Department of Energy, Office of Nuclear Energy under DOE Idaho Operations Office Contract DE-AC07-05ID14517 as part of a Nuclear Science User Facilities experiment.

DATA AVAILABILITY

The data that support the findings of this study are available from the corresponding author upon reasonable request.

[1] T. Wiss, "2.18 - Radiation effects in UO_2," in *Comprehensive Nuclear Materials*, edited by R. J. Konings (Elsevier, Oxford, 2012) pp. 465–480.

[2] M. Mogensen, N. M. Sammes, and G. A. Tompsett, "Physical, chemical and electrochemical properties of pure and doped ceria," Solid State Ion. **129**, 63–94 (2000).

[3] A. Trovarelli, C. de Leitenburg, M. Boaro, and G. Dolcetti, "The utilization of ceria in industrial catalysis," Catal. Today **50**, 353–367 (1999).

[4] E. P. Murray, T. Tsai, and S. A. Barnett, "A direct-methane fuel cell with a ceria-based anode," Nature **400**, 649–651 (1999).

[5] J. L. Bates, C. A. Hinman, and T. Kawada, "Electrical conductivity of uranium dioxide," J. Am. Ceram. Soc. **50**, 652–656 (1967).

[6] K. Shrestha, T. Yao, J. Lian, D. Antonio, M. Sessim, M. R. Tonks, and K. Gofryk, "The grain-size effect on thermal conductivity of uranium dioxide," J. Appl. Phys. **126**, 125116 (2019).

[7] B. Calés and J.F. Baumard, "Transport properties and defect structure of nonstoichiometric yttria doped ceria," J. Phys. Chem. Solids **45**, 929–935 (1984).

[8] M. Khafizov, I.-W. Park, A. Chernatynskiy, L. He, J. Lin, J. J. Moore, D. Swank, T. Lillo, S. R. Phillpot, A. El-Azab, and D. H. Hurley, "Thermal conductivity in nanocrystalline ceria thin films," J. Am. Ceram. Soc. **97**, 562–569 (2014).

[9] P. R. Hania and F. C. Klaassen, "3.04 - Thorium oxide fuel," in *Comprehensive Nuclear Materials*, edited by R. J. Konings (Elsevier, Oxford, 2012) pp. 87–108.

[10] J. S. Herring, P. E. MacDonald, K. D. Weaver, and C. Kullberg, "Low cost, proliferation resistant, uranium–thorium dioxide fuels for light water reactors," Nucl. Eng. Des. **203**, 65–85 (2001).

[11] S. F. Ashley, G. T. Parks, W.J. Nuttall, C. Boxall, and R. W. Grimes, "Thorium fuel has risks," Nature **492**, 31–33 (2012).

[12] R. Arancibia, Y. Huentupil, G. E. Buono-Core, M. Fuentealba, B. Chornik, A. Mendoza-Galván, and G. Cabello-Guzmán, "Effect of annealing temperature on the structural, morphological and optical properties of ThO_2 thin films grown by photochemical metal–organic deposition," Polyhedron **171**, 374–381 (2019).

[13] E. T. Rodine and P. L. Land, "Electronic defect structure of single-crystal ThO_2 by thermoluminescence," Phys. Rev. B **4**, 2701–2724 (1971).

[14] H. X. Song, L. Liu, H. Y. Geng, and Q. Wu, "First-principle study on structural and electronic properties of CeO_2 and ThO2 under high pressures," Phys. Rev. B **87**, 184103 (2013).

[15] M. Khafizov, J. Pakarinen, L. He, and D. H. Hurley, "Impact of irradiation induced dislocation loops on thermal conductivity in ceramics," J. Am. Ceram. Soc. **102**, 7533–7542 (2019).

[16] X.-Y. Liu, M. W. D. Cooper, K. J. McClellan, J. C. Lashley, D. D. Byler, B. D. C. Bell, R. W. Grimes, C. R. Stanek, and D. A. Andersson, "Molecular dynamics simulation of thermal transport in UO_2 containing uranium, oxygen, and fission-product defects," Phys. Rev. Applied **6**, 044015 (2016).

[17] J. T. White and A. T. Nelson, "Thermal conductivity of UO_{2+x} and U_4O_{9-y}," J. Nucl. Mater. **443**, 342–350 (2013).

[18] M. Khafizov, V. Chauhan, Y. Wang, F. Riyad, N. Hang, and D.H. Hurley, "Investigation of thermal transport in composites and ion beam irradiated materials for nuclear energy applications," J. Mater. Res. **32**, 204–216 (2017).

[19] J. Wiktor, M.-F. Barthe, G. Jomard, M. Torrent, M. Freyss, and M. Bertolus, "Coupled experimental and DFT + U investigation of positron lifetimes in UO_2," Phys. Rev. B **90**, 184101 (2014).

[20] W. F. Cureton, R. I. Palomares, C. L. Tracy, E. C. O'Quinn, J. Walters, M. Zdorovets, R. C. Ewing, M. Toulemonde, and M. Lang, "Effects of irradiation temperature on the response of CeO_2, ThO_2, and UO_2 to highly ionizing radiation," J. Nucl. Mater. **525**, 83–91 (2019).

[21] P. Martin, P. Garcia, G. Carlot, C. Sabathier, C. Valot, V. Nassif, O. Proux, and J.-L. Hazemann, "XAS characterisation of xenon bubbles in uranium dioxide," Nucl. Instrum. Meth. Phys. Res. B **266**, 2887–2891 (2008).

[22] C. Mieszczynski, G. Kuri, C. Degueldre, M. Martin, J. Bertsch, C. N. Borca, D. Grolimund, Ch. Delafoy, and E. Simoni, "Irradiation effects and micro-structural changes in large grain uranium dioxide fuel investigated by micro-beam X-ray diffraction," J. Nucl. Mater. **444**, 274–282 (2014).

[23] G. Gutierrez, C. Onofri, S. Miro, M. Bricout, and F. Leprêtre, "Effect of ballistic damage in UO_2 samples under ion beam irradiations studied by in situ raman spectroscopy," Nucl. Instrum. Meth. Phys. Res. B **434**, 45–50 (2018).

[24] P. Patsalas, S. Logothetidis, and C. Metaxa, "Optical performance of nanocrystalline transparent ceria films," Appl. Phys. Lett. **81**, 466–468 (2002).

[25] M. Khafizov, M. F. Riyad, Y. Wang, J. Pakarinen, L. He, T. Yao, A. El-Azab, and D. Hurley, "Combining mesoscale thermal transport and X-ray diffraction measurements to characterize early-stage evolution of irradiation-induced defects in ceramics," Acta Mater. **193**, 61–70 (2020).

[26] W. Chen and X.-M. Bai, "Unified effect of dispersed Xe on the thermal conductivity of UO_2 predicted by three interatomic potentials," JOM **72**, 1710–1718 (2020).

[27] C.-W. Lee, A. Chernatynskiy, P. Shukla, R.E. Stoller, S.B. Sinnott, and S.R. Phillpot, "Effect of pores and he bubbles on the thermal transport properties of UO_2 by molecular dynamics simulation," J. Nucl. Mater. **456**, 253–259 (2015).

[28] Y. Lu, Y. Yang, and P. Zhang, "Thermodynamic properties and structural stability of thorium dioxide," J. Phys. Condens. Matter **24**, 225801 (2012).

[29] J. Park, E. B. Farfán, K. Mitchell, A. Resnick, C. Enriquez, and T. Yee, "Sensitivity of thermal transport in thorium dioxide to defects," J. Nucl. Mater. **504**, 198–205 (2018).

[30] J. M. Mann, D. Thompson, K. Serivalsatit, T. M. Tritt, J. Ballato, and J. Kolis, "Hydrothermal growth and thermal property characterization of ThO_2 single crystals," Cryst. Growth Des. **10**, 2146–2151 (2010).

[31] R. I. Palomares, C. L. Tracy, F. Zhang, C. Park, D. Popov, C. Trautmann, R. C. Ewing, and M. Lang, "*In situ* defect annealing of swift heavy ion irradiated CeO_2 and ThO_2 using synchrotron X-ray diffraction and a hydrothermal diamond anvil cell," J. Appl. Crystallogr. **48**, 711–717 (2015).

[32] R. I. Palomares, C. L. Tracy, J. Neuefeind, R. C. Ewing, C. Trautmann, and M. Lang, "Thermal defect annealing of swift heavy ion irradiated ThO_2," Nucl. Instrum. Method. Phys. Res. B **405**, 15–21 (2017).

[33] H. Y. Xiao and W. J. Weber, "Oxygen vacancy formation and migration in $Ce_xTh_{1-x}O_2$ solid solution," J. Phys. Chem. B **115**, 6524–6533 (2011).

[34] Y. Yun, P. M. Oppeneer, H. Kim, and K. Park, "Defect energetics and Xe diffusion in UO_2 and ThO_2," Acta Mater. **57**, 1655–1659 (2009).

[35] D. H. Hurley, R. S. Schley, M. Khafizov, and B. L. Wendt, "Local measurement of thermal conductivity and diffusivity," Rev. Sci. Instrum. **86**, 123901 (2015).

[36] M. Khafizov, C. Yablinsky, T. R. Allen, and D. H. Hurley, "Measurement of thermal conductivity in proton irradiated silicon," Nucl. Instrum. Meth. Phys. Res. B **325**, 11–14 (2014).

[37] L. He, M. Gupta, C. A. Yablinsky, J. Gan, M. A. Kirk, X.-M. Bai, J. Pakarinen, and T. R. Allen, "In situ TEM observation of dislocation evolution in Kr-irradiated UO_2 single crystal," J. Nucl. Mater. **443**, 71–77 (2013).

[38] J. Pakarinen, M. Khafizov, L. He, C. Wetteland, J. Gan, A. T. Nelson, D. H. Hurley, A. El-Azab, and T. R. Allen, "Microstructure changes and thermal conductiv-

ity reduction in UO_2 following 3.9 MeV He^{2+} ion irradiation," J. Nucl. Mater. **454**, 283–289 (2014).

[39] H. Y. Xiao, Y. Zhang, and W. J. Weber, "Ab initio molecular dynamics simulations of low-energy recoil events in ThO_2, CeO_2, and ZrO_2," Phys. Rev. B **86**, 054109 (2012).

[40] W. J. Weber and Y. Zhang, "Predicting damage production in monoatomic and multi-elemental targets using stopping and range of ions in matter code: Challenges and recommendations," Curr. Opin. Solid State Mater. Sci. **23**, 100757 (2019).

[41] J. F. Ziegler, M. D. Ziegler, and J. P. Biersack, "SRIM: The stopping and range of ions in matter (2010)," Nucl. Instrum. Meth. Phys. Res. B **268**, 1818–1823 (2010).

[42] A. A. Maznev, J. Hartmann, and M. Reichling, "Thermal wave propagation in thin films on substrates," J. Appl. Phys. **78**, 5266–5269 (1995).

[43] J. S. Hwang, K. J. Lin, and C. Tien, "Measurement of heat capacity by fitting the whole temperature response of a heat-pulse calorimeter," Rev. Sci. Instrum. **68**, 94–101 (1997).

[44] F. A. McDonald, "Photoacoustic effect and the physics of waves," Am. J. Phys. **48**, 41–47 (1980).

[45] D. G. Cahill, "Thermal-conductivity measurement by time-domain thermoreflectance," MRS Bull. **43**, 782–789 (2018).

[46] M. F. Riyad, V. Chauhan, and M. Khafizov, "Implementation of a multilayer model for measurement of thermal conductivity in ion beam irradiated samples using a modulated thermoreflectance approach," J. Nucl. Mater. **509**, 134–144 (2018).

[47] Z. Hua, A. Fleming, and H. Ban, "The study of using a multi-layered model to extract thermal property profiles of ion-irradiated materials," Int. J. Heat Mass Transf. **131**, 206–216 (2019).

[48] C. A. Schneider, W. S. Rasband, and K. W. Eliceiri, "NIH image to ImageJ: 25 years of image analysis," Nat. Meth. **9**, 671–675 (2012).

[49] K. Iakoubovskii, K. Mitsuishi, Y. Nakayama, and K. Furuya, "Thickness measurements with electron energy loss spectroscopy," Microsc. Res. Tech. **71**, 626–631 (2008).

[50] K. Rickert, T. A. Prusnick, M. M. Kimani, E. A. Moore, C. A. Merriman, and J. M. Mann, "Assessing UO_2 sample quality with µ-raman spectroscopy," J. Nucl. Mater. **514**, 1–11 (2019).

[51] Z.-M. Zhang, S. Chen, and Y.-Z. Liang, "Baseline correction using adaptive iteratively reweighted penalized least squares," Analyst **135**, 1138–1146 (2010).

[52] C. J. Ulmer and A. T. Motta, "Characterization of faulted dislocation loops and cavities in ion irradiated alloy 800H," J. Nucl. Mater. **498**, 458–467 (2018).

[53] V. S. Chauhan, J. Pakarinen, T. Yao, L. He, D. H. Hurley, and M. Khafizov, "Comprehensive characterization of irradiation induced defects in ceria: Impact of point defects on vibrational and optical properties," (2020), Submitted.

[54] V. G. Keramidas and W. B. White, "Raman spectra of oxides with the fluorite structure," J. Chem. Phys. **59**, 1561 (1973).

[55] T. Livneh and E. Sterer, "Effect of pressure on the resonant multiphonon raman scattering in UO_2," Phys. Rev. B **73**, 085118 (2006).

[56] J. Lv, G. Li, S. Guo, and Y. Shi, "Raman scattering from phonons and electronic excitations in UO_2 with different oxygen isotopes," J. Raman Spec. **47**, 345–349 (2016).

[57] L. Desgranges, G. Baldinozzi, P. Simon, G. Guimbretière, and A. Canizares, "Raman spectrum of U_4O_9: a new interpretation of damage lines in UO_2," J. Raman Spec. **43**, 455–458 (2012).

[58] D. Manara and B. Renker, "Raman spectra of stoichiometric and hyperstoichiometric uranium dioxide," J. Nucl. Mater. **321**, 233–237 (2003).

[59] J. M. Elorrieta, L. J. Bonales, N. Rodrigues-Villagra, V. G. Baonza, and J. Cobos, "A detailed raman and X-ray study of UO_{2+x} oxides and related structure transitions," Phys. Chem. Chem. Phys. **18**, 28209–28216 (2016).

[60] P. R. Graves, "Raman microprobe spectroscopy of uranium dioxide single crystals and ion implanted polycrystals," Appl. Spectrosc. **44**, 1665–1667 (1990).

[61] G. Guimbretière, L. Desgranges, A. Canizares, G. Carlot, R. Caraballo, C. Jégou, F. Duval, N. Raimboux, M. R. Ammar, and P. Simon, "Determination of in-depth damage profile by raman line scan on pre-cut He^{2+} irradiated UO_2," Appl. Phys. Lett. **100**, 251914 (2012).

[62] Z. Talip, T. Wiss, P.E. Raison, J. Paillier, D. Manara, J. Somer, and R. J. M. Konings, "Raman and X-ray studies of uranium-lanthanum-mixed oxides before and after air oxidation," J. Am. Ceram. Soc. **98**, 2278–2285 (2015).

[63] C. L. Tracy, J. M. Pray, M. Lang, D. Popov, C. Park, C. Trautmann, and R. C. Ewing, "Defect accumulation in ThO_2 irradiated with swift heavy ions," Nucl. Instrum. Method. Phys. Res. B **326**, 169–173 (2014).

[64] R. I. Palomares, J. Shamblin, C. L. Tracy, J. Neuefeind, R. C. Ewing, C. Trautmann, and M. Lang, "Defect accumulation in swift heavy ion-irradiated CeO_2 and ThO_2," J. Mater. Chem. A **5**, 12193 (2017).

[65] H. Y. Xiao, Y. Zhang, and W. J. Weber, "Stability and migration of charged oxygen interstitials in ThO_2 and CeO_2," Acta Mater. **61**, 7639–7645 (2013).

[66] S. T. Murphy, M. W. D. Cooper, and R. W. Grimes, "Point defects and non-stoichiometry in thoria," Solid State Ion. **267**, 80–87 (2014).

[67] M. Jin, C. Jiang, J. Gan, and D. H. Hurley, "Systematic analysis on the primary radiation damage in $Th_{1-x}U_xO_2$ fluorite systems," J. Nucl. Mater. **536**, 152144 (2020).

[68] S. Knight, R. Korlacki, C. Dugan, J. C. Petrosky, A. Mock, P. A. Dowben, J. M. Mann, M. M. Kimani, and M. Schubert, "Infrared-active phonon modes in single-crystal thorium dioxide and uranium dioxide," J. Appl. Phys. **127**, 125103 (2020).

[69] A. Nakajima, A. Yoshihara, and M. Ishigame, "Defect-induced raman spectra in doped CeO_2," Phys. Rev. B **50**, 13297–13307 (1994).

[70] C. Schilling, A. Hofmann, C. Hess, and M. V. Ganduglia-Pirovano, "Raman spectra of polycrystalline CeO_2: a density functional theory study," J. Phys. Chem. C **121**, 20834–20849 (2017).

[71] L. Desgranges, G. Guimbretiére, P. Simon, C. Jegou, and R. Caraballo, "A possible new mechanism for defect formation in irradiated UO_2," Nucl. Instrum. Meth. Phys. Res. B **315**, 169–172 (2013).

[72] R. Mohun, L. Desgranges, C. Jégou, B. Boizot, O. Cavani, A. Canizarés, F. Duval, C. He, P. Desgardin, M.-F. Barthe, and P. Simon, "Quantification of irradiation-induced defects in UO_2 using raman and positron annihilation spectroscopies," Acta Mater. **164**, 512–519 (2019).

[73] L. Desgranges, G. Guimbretiére, P. Simon, F. Duval, A. Canizares, R. Omnee, C. Jégou, and R. Caraballo, "Annealing of the defects observed by raman spectroscopy in UO_2 irradiated by 25 MeV He^{2+} ions," Nucl. Instru. Meth. Phys. Res. B **327**, 74–77 (2014).

[74] E. Villa-Aleman, N. J. Bridges, T. C. Shehee, and A. L. Houk, "Raman microspectroscopy of PuO_2 particulate aggregates," J. Nucl. Mater. **515**, 140–149 (2019).

[75] J. Lee, J. Kim, Y.-S. Youn, N. Liu, J.-G. Kim, Y.-K. Ha, D. W. Shoesmith, and J.-Y. Kim, "Raman study on structure of $U_{1-y}Gd_yO_{2-x}$ (y=0.005, 0.01, 0.03, 0.05 and 0.1) solid solutions," J. Nucl. Mater. **486**, 216–221 (2017).

[76] R. Mohun, L. Desgranges, J. Léchelle, P. Simon, G. Guimbretière, A. Canizares, F. Duval, C. Jégou, M. Magnin, N. Clavier, N. Dacheux, C. Valot, and R. Vauchy, "Charged defects during alpha-irradiation of actinide oxides as revealed by raman and luminescence spectroscopy," Nucl. Instrum. Method. Phys. Res. B **374**, 67–70 (2016).

[77] T. R. Griffiths and J. Dixon, "Electron irradiation of single crystal thorium dioxide and electron transfer reactions," Inorganica Chimica Acta **300–302**, 305–313 (2000).

[78] H. Y. Geng, Y. Chen, Y. Kaneta, M. Iwasawa, T. Ohnuma, and M. Kinoshita, "Point defects and clustering in uranium dioxide by LSDA + U calculations," Phys. Rev. B **77**, 104120 (2008).

[79] C. Matthews, R. Perriot, M. W. D. Cooper, C. R. Stanek, and D. A. Andersson, "Cluster dynamics simulation of uranium self-diffusion during irradiation in UO_2," J. Nucl. Mater. **527**, 151787 (2019).

[80] S. E. Ferry, C. A. Dennett, K. B. Woller, and M. P. Short, "Inferring radiation-induced microstructural evolution in single-crystal niobium through changes in thermal transport," J. Nucl. Mater. **523**, 378–382 (2019).

[81] W.-Y. Chen, J. Wen, M. A. Kirk, Y. Miao, B. Ye, B. R. Kleinfeldt, A. J. Oaks, and J. F. Stubbins, "Characterization of dislocation loops in CeO_2 irradiated with high energy krypton and xenon," Phil. Mag. **93**, 4569–4581 (2013).

[82] L. W. Hobbs, A. E. Hughes, D. Pooley, and Peter Bernhard Hirsch, "A study of interstitial clusters in irradiated alkali halides using direct electron microscopy," Proc. R. Soc. A **332**, 167–185 (1973).

[83] C. Onofri, C. Sabathier, C. Baumier, C. Bachelet, H. Palancher, and M. Legros, "Evolution of extended defects in polycrystalline Au-irradiated UO_2 using in situ TEM: Temperature and fluence effects," J. Nucl. Mater. **482**, 105–113 (2016).